JEM Journal of Experimental Medicine

BRIEF DEFINITIVE REPORT

Single-cell imaging of CAR T cell activity in vivo reveals extensive functional and anatomical heterogeneity

Marine Cazaux[1,2*], Capucine L. Grandjean[1*], Fabrice Lemaître[1], Zacarias Garcia[1], Richard J. Beck[3], Idan Milo[1], Jérémy Postat[1,2], Joost B. Beltman[3], Eleanor J. Cheadle[4], and Philippe Bousso[1]

CAR T cells represent a potentially curative strategy for B cell malignancies. However, the outcome and dynamics of CAR T cell interactions in distinct anatomical sites are poorly understood. Using intravital imaging, we tracked interactions established by anti-CD19 CAR T cells in B cell lymphoma–bearing mice. Circulating targets trapped CAR T cells in the lungs, reducing their access to lymphoid organs. In the bone marrow, tumor apoptosis was largely due to CAR T cells that engaged, killed, and detached from their targets within 25 min. Notably, not all CAR T cell contacts elicited calcium signaling or killing while interacting with tumors, uncovering extensive functional heterogeneity. Mathematical modeling revealed that direct killing was sufficient for tumor regression. Finally, antigen-loss variants emerged in the bone marrow, but not in lymph nodes, where CAR T cell cytotoxic activity was reduced. Our results identify a previously unappreciated level of diversity in the outcomes of CAR T cell interactions in vivo, with important clinical implications.

Introduction

Chimeric antigen receptor (CAR) T cells represent a potentially curative strategy for B cell malignancies. In recent clinical trials, CAR T cells targeting the CD19 molecule have demonstrated remarkable activity in the treatment of B cell leukemias and B cell lymphomas (Maude et al., 2014; Neelapu et al., 2017; Schuster et al., 2017; Park et al., 2018). Despite these promising results, the cellular interactions regulating anti-CD19 CAR T cell activity and tumor regression in vivo are incompletely understood. First, CAR T cells may interact with target cells in various anatomical sites and these contacts may potentially modulate their activity and persistence. In this respect, CAR T cell numbers are influenced by endogenous B cells (Cheadle et al., 2010), which can favor their accumulation in the lung (James et al., 2009), although the underlying mechanism remains to be characterized. Second, cellular interactions leading to tumor regression are not fully understood. CAR T cell killing dynamics have been analyzed in vitro (Davenport et al., 2015, 2018; Liadi et al., 2015), but not in vivo, limiting our understanding of the quantitative and qualitative requirements for CAR T cell–mediated tumor regression. Another key unanswered question is whether tumor regression is primarily the result of direct CAR T cell killing or whether CAR T cells largely act by activating other host immune cells at the tumor site (Barber et al., 2009; Chmielewski et al., 2011; Yeku et al., 2017). Finally, CAR T cell therapy has been shown to favor the emergence of CD19-negative tumors in some patients (Grupp et al., 2013; Maude et al., 2014; Sotillo et al., 2015; Gardner et al., 2016; Jacoby et al., 2016; Ruella and Maus, 2016), but the anatomical sites of tumor escape have yet to be characterized.

To address these important questions, we visualized CAR T cell activity in a mouse model of B cell aggressive lymphoma using intravital imaging and a genetically encoded reporter for apoptosis. CAR T cells that interacted with circulating targets were trapped in the lungs in the form of large cell aggregates. At the tumor site, CAR T cells exhibited extensive functional heterogeneity but harbored the potential to rapidly kill their targets, directly accounting for tumor regression. Finally, we uncovered anatomical differences in tumor immunoediting associated with distinct levels of cytotoxic activity. Thus, the outcomes of CAR T cell interactions in vivo are highly diverse

[1]Dynamics of Immune Responses Unit, Equipe Labellisée Ligue Contre le Cancer, Institut Pasteur, INSERM U1223, Paris, France; [2]University Paris Diderot, Sorbonne Paris Cité, Cellule Pasteur, Paris, France; [3]Division of Drug Discovery and Safety, Leiden Academic Centre for Drug Research, Leiden University, Leiden, Netherlands; [4]Targeted Therapy Group, Manchester Cancer Research Centre, Division of Cancer Sciences, School of Medical Sciences, Faculty of Biology, Medicine and Health, The University of Manchester, Manchester Academic Health Sciences Centre, Manchester, UK.

*M. Cazaux and C.L. Grandjean contributed equally to this paper; Correspondence to Philippe Bousso: philippe.bousso@pasteur.fr.

and influenced both by functional properties and anatomical specificities.

Results and discussion

Detecting CAR T cell–mediated killing using a genetically encoded apoptosis reporter

To establish a mouse model of CAR T cell therapy, we used a tumor cell line derived from a Eμ-myc transgenic mouse that develops spontaneous Burkitt-like B cell lymphoma (Adams et al., 1985; Harris et al., 1988). These cells expressed the CD19 marker, and when injected into recipient mice, established in the bone marrow, spleen, and lymph nodes. With the aim to delineate the cytotoxicity of CAR T cells, we generated anti-CD19 CAR T cells by retroviral transduction of activated mouse CD8$^+$ T cells. These cells efficiently recognized Eμ-myc tumor cells in vitro, leading to their up-regulation of granzyme B and programmed cell death–1 (PD-1) and the production of IFN-γ. These hallmarks of activation were not detected in control untransduced activated CD8$^+$ T cells or when CAR T cells were cultured without targets (Fig. S1, A and B). As a mean to detect tumor cell apoptosis in real time, we expressed a genetically encoded fluorescence resonance energy transfer (FRET)–based reporter for caspase-3 activity in Eμ-myc tumor cells (Fig. S1 C). This reporter is based on the fusion of the CFP and YFP linked by the caspase-3 target peptide DEVD (Breart et al., 2008; Garrod et al., 2012). Caspase-3 activity results in the cleavage of the probe and in loss of FRET. Using flow cytometry, we found that CAR T cells efficiently induced tumor cell apoptosis as measured by FRET loss in malignant B cells (Fig. S1, D and E), resulting in the elimination of virtually all tumor cells within a day (Fig. S1 F). Tumor cell apoptosis could also be readily detected using in vitro time-lapse imaging following contacts with CAR T cells (Fig. S1 G). These results established a relevant model to study and visualize CAR T cell cytotoxic activity in vivo.

CAR T cells are trapped in the lung following clustering with tumor cells

We next thought to study cellular interactions regulating CAR T cell engraftment/persistence. A previous study that used anti-CD20 CAR T cells reported that CAR T cells failed to home to the bone marrow in the presence of endogenous B cells and instead accumulated in the lungs (James et al., 2009). Using anti-CD19 CAR T cells, we also observed that B cell depletion or the use of B cell–deficient mice promoted CAR T cell accumulation in the bone marrow (Fig. 1 A). To gain insight into the underlying mechanism, we imaged the lungs of recipient mice within 15 min of CAR T cell injection. As shown in Fig. 1 B, numerous large cellular clusters containing both CAR T and B cells were detected. This observation suggests that CAR T cells interact with B cells as they enter the circulation, resulting in the formation of large cellular aggregates that are trapped in the lungs. We next asked whether, in the context of an established B cell malignancy, circulating tumors may also favor CAR T cell trapping in the lungs. This is particularly relevant, as some patients with B cell lymphoma/leukemia can exhibit high circulating tumor burden. To address this question, RAG2$^{-/-}$ mice were conditioned with a sublethal dose of irradiation and then injected or not with Eμ-myc cells. Animals were treated with CAR T cells once circulating tumors cells became detectable in blood (typically 10 d later). We found that, rapidly after transfer, CAR T cells trafficking to the bone marrow was largely altered in tumor bearing mice (Fig. 1 C). The lack of homing to the bone marrow was associated with the rapid accumulation of cellular aggregates containing CAR T cells and tumor cells in the lungs (Fig. 1, D and E). By contrast, these large cellular aggregates were absent from the lungs of RAG2$^{-/-}$ mice lacking CD19 expressing cells (Fig. 1, D and E). To confirm that these large cellular aggregates formed in the circulation, we coinjected tumor, CAR, and control T cells in naive recipients and imaged the lungs 15 min later. Cellular clusters comprising CAR T cells and tumors accumulated in the lung microcirculation already at this early time point, emphasizing the role of circulating targets (Fig. 1 F). In these experiments, CAR T cells accumulated in the lungs twice as much as control CD8$^+$ T cells, indicating that trapping by circulating tumors was dependent on CAR-mediated interactions. Although it remains possible that this trapping phenomenon is transient, our results indicate that the presence of B cells limits CAR T cell engraftment in the bone marrow for at least 3 d (Fig. 1 A). To test the functional consequence of CAR T cell trapping by circulating targets (B cells and tumors), we thought to reduce circulating targets using anti-CD20 antibody. Importantly, our tumor cells expressed very low levels of CD20 (Fig. S2 A) and were not depleted by anti-CD20 treatment in contrast to B cells (Fig. S2, B–D). By specifically depleting B cells, this strategy enabled the removal of a fraction of circulating targets with minimal direct antitumor effect. The combination of CAR T cells and anti-CD20 therapy significantly reduced the tumor burden (Fig. S2 D) and was associated with a moderately prolonged survival (Fig. S2 E). Our results, extending those of a prior study (James et al., 2009), suggest that circulating targets (B cells and tumor cells) may represent a substantial hurdle for CAR T cell therapy by outcompeting bone marrow tumor cells and/or physically sequestrating CAR T cells in the lung.

CAR T cells exhibit rapid killing dynamics in the bone marrow

We next investigated the extent to which CAR T cells kill malignant B cells in the bone marrow, a primary site of B cell lymphoma/leukemia development. Based on our results on CAR T cell engraftment, CAR T cells were transferred into preconditioned lymphoma-bearing mice when the disease was largely restricted to the bone marrow with minimal circulating tumors. Using intravital two-photon imaging, we found that 2 d after transfer, both CAR T cells and control untransduced activated CD8$^+$ T cells were detectable in the bone marrow (Fig. 2 A and Video 1). Notably, the presence of apoptotic tumor cells was largely restricted to recipients treated with CAR T cells (Fig. 2, A and B). To characterize CAR T cell killing dynamics and establish the fraction of tumor cells that was eliminated as a direct consequence of a cellular interaction with CAR T cells, we performed real-time imaging, focusing on tumor cells that underwent apoptosis (as measured by FRET loss) during the imaging period. We observed that most tumor apoptotic events (73%) occurred in the context of a direct cellular contact with a

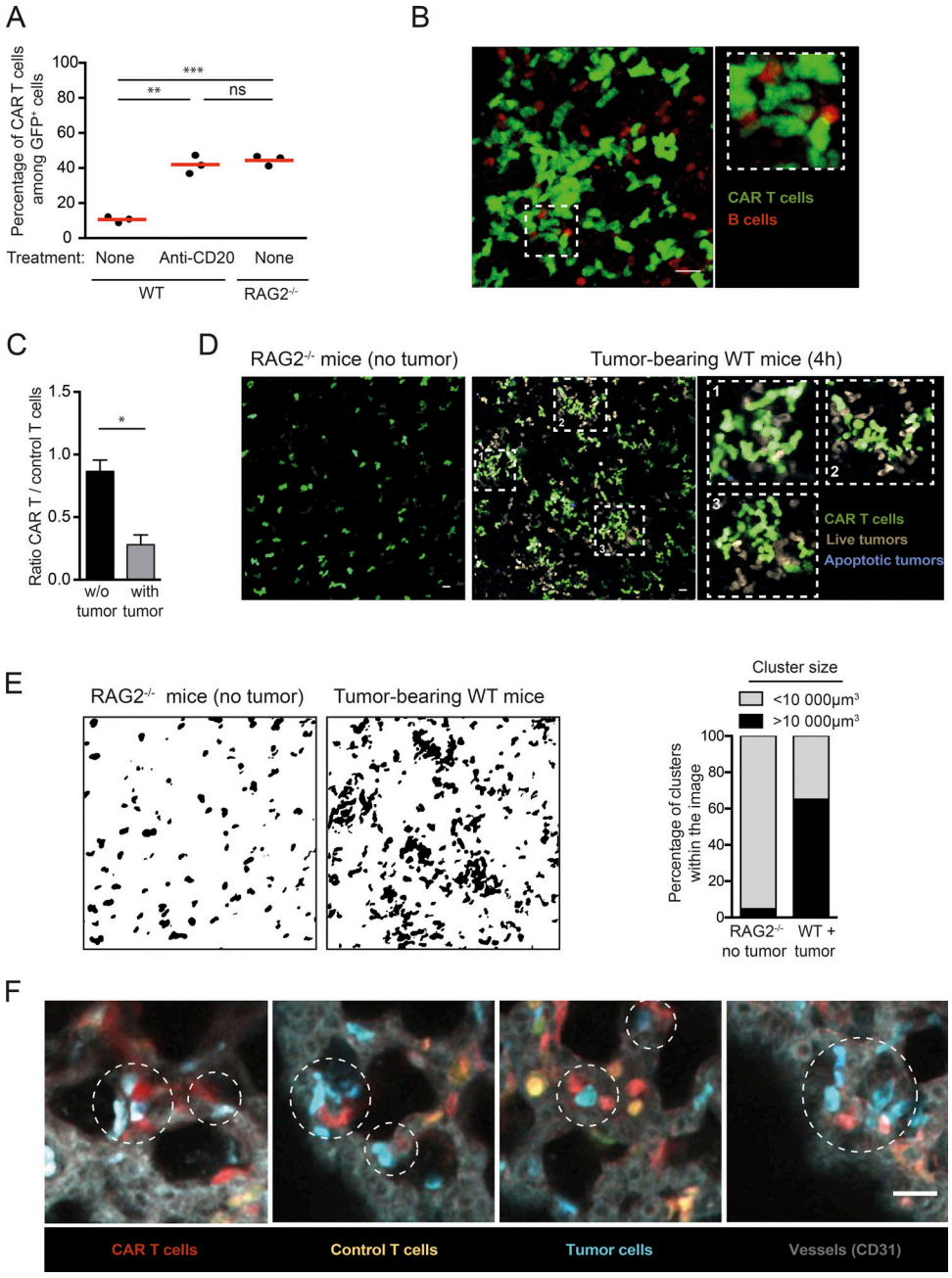

Figure 1. **Cellular aggregates formed between CAR T cells and circulating tumors accumulate in the lungs. (A)** Endogenous B cells limit CAR T cell accumulation in the bone marrow. RAG2$^{-/-}$ or C57BL/6 mice were injected with a mixture of CAR^{+} and CAR^{-} GFP^{+} T cells (containing 60% CAR^{+} T cells). One group of mice was treated 3 d before with 50 µg anti-CD20 mAb i.v. The percentage of CAR^{+} T cells (as detected by hCD34 expression) among GFP^{+} cells was assessed in the bone marrow 3 d after T cell transfer using flow cytometry. Red horizontal bars represent mean values. Representative of two independent experiments (n = 3 mice per group). Unpaired t test was used for statistical analysis. **, P < 0.01; ***, P < 0.001; ns, not significant. **(B)** CAR T cells form clusters with B cells. Representative two-photon images of the lungs 15 min after CAR T cell injection in CD19-RFP recipients showing the presence of large cellular aggregates containing CAR T cells (green) and B cells (red). Representative of two independent experiments. Scale bar represents 20 µm. **(C)** RAG2$^{-/-}$ mice were conditioned by irradiation (4 Gy) and injected (or not) with Eµ-myc cells. After 2 wk, 10 × 10^{6} CAR T cells and 10 × 10^{6} control T cells were coinjected i.v., and their trafficking to the bone marrow was assessed 4 h later by flow cytometry. Four mice per group were analyzed in two independent experiments. Mann–Whitney test was used for statistical analysis. *, P < 0.05. **(D and E)** CAR T cells form clusters with tumor cells. Mice were conditioned by irradiation (4 Gy) and injected with Eµ-myc-DEVD cells. After 10 d, 10 × 10^{6} CAR T cells were injected i.v. We used untreated RAG2$^{-/-}$ mice as control recipients that did not contain any CD19^{+} targets. **(D)** Representative two-photon images of the lungs showing that CAR T cells form cell aggregates in tumor-bearing mice, but not in control RAG2$^{-/-}$ recipients. Representative of two independent experiments. **(E)** Quantification of cluster volume in the indicated recipients. The graph shows the percentage of clusters calculated to be >10,000 µm^{3}. **(F)** CAR T cells and circulating tumor cells formed clusters that accumulated in the lungs. RAG2$^{-/-}$ mice were adoptively transferred with a 1:1 mixture of dye-labeled CAR T cells and control untransduced T cells and 5 min later with tumor cells i.v. Two-photon imaging of the explanted lungs was performed 15 min later. Representative images showing that CAR T cells (red) and tumor cells (blue) in the circulation formed cellular aggregates detected within minutes in the lungs. Control T cells were not clustered and are shown in orange. Vessels (gray) were visualized by i.v. injection of a PE-conjugated anti-CD31 mAb. Representative of 12 images in two independent experiments. Scale bar represents 20 µm.

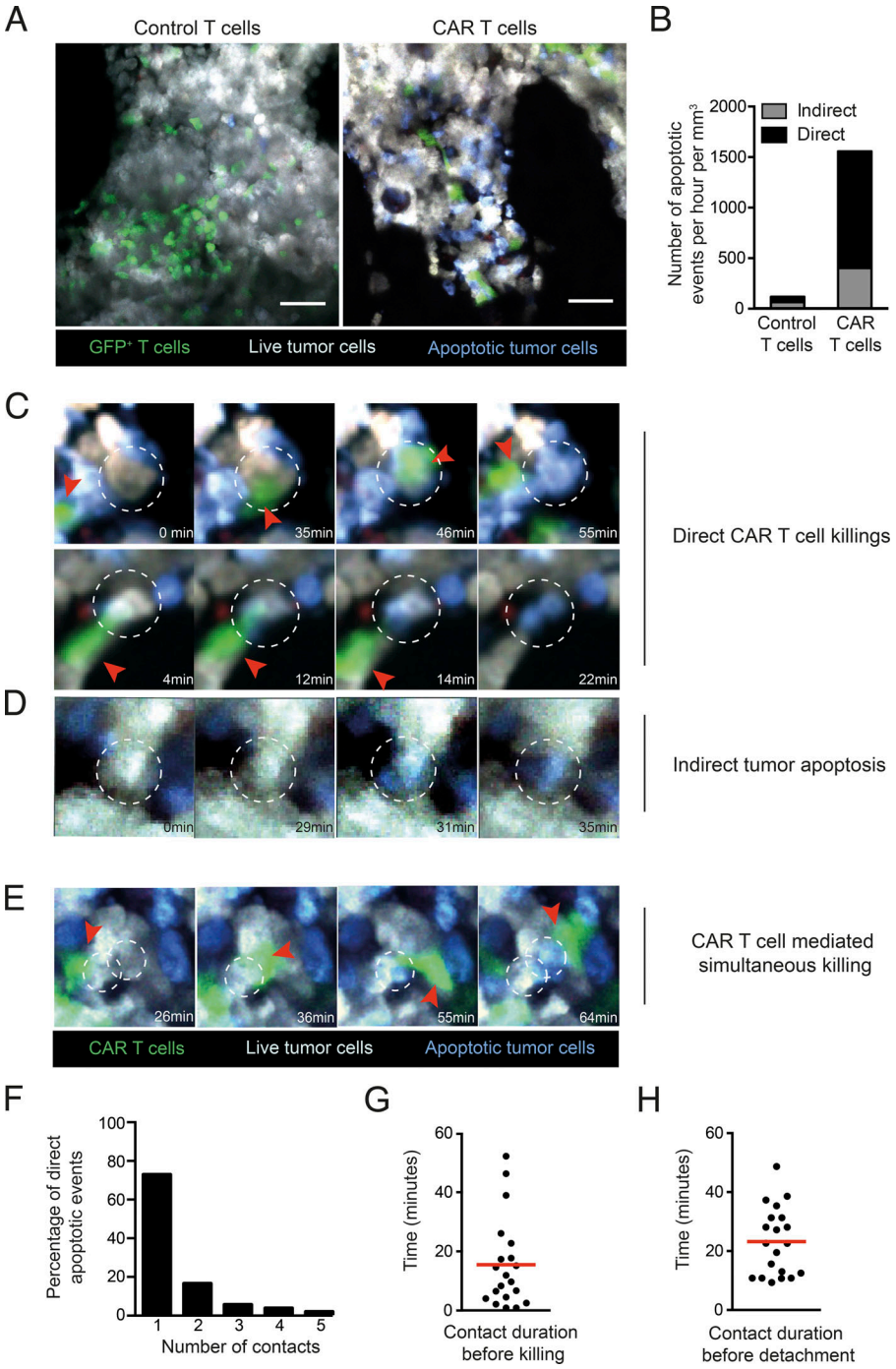

Figure 2. **Intravital imaging of CAR T cell dynamics and cytotoxicity in the bone marrow in mice with established B cell lymphoma.** B cell lymphomas were established by i.v. injection of 0.5 × 10^6 Eμ-myc-DEVD cells in C57BL/6 mice after sublethal irradiation (4 Gy). 7 d later, mice were injected i.v. with 20 × 10^6 purified CAR T cells or control activated T cells (untransduced). Bone marrow intravital imaging was performed 40 h after T cell transfer. **(A)** Representative two-photon images of tumor-bearing mice treated with GFP+ control or CAR T cells. T cells are shown in green, live tumor cells in gray, and apoptotic tumor cells in blue. Scale bars represent 50 μm. **(B)** Quantification of tumor apoptotic events per hour per mm^3 of imaging volume. Events in which tumors became apoptotic during the imaging period were recorded. Apoptotic events were considered as direct killing (n = 55) when a CAR T cell engaged the tumor cells before the detection of FRET loss. Indirect events (n = 20) corresponded to tumor cells undergoing FRET loss without any apparent interactions with a CAR T cell during the imaging period. **(C and D)** Representative time-lapse images showing examples of tumor apoptosis. **(C)** Representative time-lapse images showing two examples of direct CAR T cell killing. **(D)** Time-lapse images illustrating tumor apoptosis in the absence of apparent contact with CAR T cells. **(E)** Example of two adjacent tumor cells undergoing apoptosis sequentially upon CAR T cell contact. CAR T cells (green) are highlighted by red arrowheads, and dotted circles show tumor cells undergoing apoptosis. **(F)** For direct killing events, we counted the number of CAR T cells seen contacting the tumor cell before apoptosis. For 73% of the direct killing events, a single CAR T cell was seen interacting with the tumor cell during the imaging period. **(G and H)** Quantification of CAR T cell killing dynamics. For each direct killing event for which CAR T cell attachment and detachment was visualized, we measured time from T cell contact with tumor cells to killing (G) and T cell detachment (H). Mean durations are shown by red horizontal bars. All data shown were representative of 10 movies for control T cells and 17 movies for CAR T cells performed in three independent experiments.

CAR T cell (Fig. 2, B and C; and Videos 2 and 3). Of note, the transfer of CAR T cells also increased by 6.5-fold the number of indirect killing events (Fig. 2 B), in which tumor cells underwent apoptosis in the absence of any detectable interactions with CAR T cells (Fig. 2 D and Video 4). While we cannot exclude that CAR T cells interacted with these tumor cells before we started imaging, these indirect apoptosis events may reflect a boost in the activity of endogenous effectors and/or an activity of CAR T cell–derived cytokines.

In most direct killing events, a single CAR T cell could be detected in interaction with one target cell (Fig. 2 F). For the majority of direct killing events, we could quantify the time from target engagement to FRET loss and to target detachment. Overall, killing was rapid and dynamic as CAR T cells engaged, killed, and detached from their target in ∼25 min (Fig. 2, G and H). We cannot exclude that a fraction of CAR T cells may interact for longer periods during killing due to the constrained duration of imaging (1–2 h). Thus, despite expressing a high affinity receptor, anti-CD19 CAR T cells were able to detach rapidly and quickly resume motility, a property that should favor serial killing. Consistent with this idea, in a few instances, we observed evidence for killing of adjacent tumors cells by a single CAR T cell (Fig. 2 E and Video 5). To further confirm the high killing capacity of CAR T cells, we compared their activity to

those of regular CTLs analyzed in the most favorable context (high-affinity TCR and tumor overexpressing the cognate antigen). Specifically, we analyzed activated T cells expressing the high-affinity OT-I TCR against the same tumor transduced to express high levels of OVA. In vitro and in vivo, CAR T cells exhibited similar, if not higher anti-tumor activity compared with OT-I T cells (Fig. S3). Overall, our results demonstrate that CAR T cell cytotoxic activity plays a major and direct role in tumor elimination and that rapid killing dynamics in vivo are a hallmark of CAR T cells.

Functional heterogeneity in CAR T cell–tumor interactions in the bone marrow

While our imaging experiments revealed that CAR T cell–mediated tumor killing is a highly rapid event, not all CAR T cell interactions led to target killing. On average, ∼20% of CAR T cells were engaged in a killing event during the imaging period (Fig. 3 A). A fraction of CAR T cells were seen interacting and detaching from their target without triggering apoptosis (Fig. 3 B and Video 6). Such heterogeneity in outcome may originate from cell–cell variability in cytotoxic potential among CAR T cells (e.g., variability in cytotoxic granules contents). Alternatively, differences in CAR T cell signaling upon contact could result in distinct functional consequences. To test the latter hypothesis, we focused on Ca^{2+} signals that are important for both conjugate formation and the release of cytotoxic granules. CAR T cells expressing the Twitch2B calcium indicator were imaged in mice harboring tumors expressing the caspase-3 reporter (Fig. 3 C). As illustrated in Fig. 3, D and E, and Videos 7 and 8, some CAR T cells exhibited a strong calcium response upon contact with tumors cells, while others were poorly responsive despite forming prolonged contacts. In addition, while killing was associated with a robust calcium elevation in the CAR T cell, some interactions led to a detectable calcium response without apparent killing. To test whether the lack of signaling seen in some CAR T cells was due to a defect in CAR recognition or a more general block in the calcium pathway, we designed an experiment to stimulate CAR T cells via their endogenous TCR in vivo. CAR T cells were prepared from OT-I $CD8^+$ T cells and imaged in the bone marrow of tumor-bearing mice (Fig. 3 F). Injection of $OVA^{257–264}$ peptide led to a robust calcium response in all CAR T cells, suggesting that CAR T cells remained competent for calcium response (Fig. 3 G). This result supports the idea that nonresponding CAR T cells exhibit an altered CAR-mediated signaling that does not originate from a global block in calcium mobilization. Altogether, these experiments uncovered an extensive heterogeneity in signaling during individual CAR T cell–tumor interactions that impacts killing outcome.

CAR T cell direct activity mediates the rapid clearance of tumor cells from the bone marrow

The occurence of indirect apoptotic events at the tumor site raises the question of whether these events play a major role in tumor regression. When we analyzed the bone marrow on day 5 after CAR therapy, we observed that the vast majority of tumor cells had been eliminated as detected by intravital imaging and flow cytometry (Fig. 4, A–D). We also found that the density of CAR T cells increased by ∼10-fold between day 2 and day 5 (Fig. 4 E). Finally, the percentage of apoptotic tumor cells detected ex vivo by flow cytometry using our reporter system increased between day 2 and day 5 and was largely correlated with the percentage of CAR T cells present in the bone marrow (Fig. 4 F).

To assess whether direct CAR T cell killing is sufficient to explain the clearance of tumor cells or whether additional recruited effectors play a determinant role, we took advantage of our experimental measurements of killing dynamics to establish a mathematical model of tumor outcome. In particular, we calculated the rate of CAR T cell killing (implying a direct contact) and the observed increase in CAR T cell numbers between day 2 and day 5 from intravital datasets. Tumor growth was described with the Gompertz model (Murphy et al., 2016), implying that tumor growth progressively slows down (e.g., because of the confined space) but may increase due to cleared bone marrow niches during CAR T cell–mediated tumor regression. As shown in Fig. 4 G, these simulations supported the idea that direct CAR T cell activity was sufficient to clear the vast majority of tumor cells in a few days. Importantly, these results held true for a wide range of initial tumor growth rate at the time of CAR T cell transfer (Fig. 4 G). Moreover, the modeling showed that the observed killing rate per CAR T cell was critical for tumor regression (Fig. 4 H). In addition, relatively small differences in early CAR T cell infiltration in the bone marrow substantially impact tumor outcome (Fig. 4 H). This observation emphasizes the detrimental role that CAR T cell trapping by circulating targets may have on tumor clearance.

Thus, intravital imaging and mathematical modeling support the idea that CAR T cells can solely rely on their direct cytotoxicity activity rather than on the recruitment and activation of other effectors to eliminate the bulk of the B cell lymphoma in the bone marrow within a few days.

Tumor relapse coincides with CAR T cell disappearance and immunoediting

Recipient mice treated with CAR T cells exhibited a significantly prolonged survival but ultimately relapsed (Fig. 5 A). By day 21 after therapy, the bone marrow was invaded with tumor cells (Fig. 5 B). At this time, almost no CAR T cells and very few apoptotic tumors were detected in the bone marrow, indicating the absence of ongoing cytotoxic immune response. CAR T cells became largely undetectable in the bone marrow and lymph nodes 4 wk after therapy (Fig. 5 C). Similar to what has been observed in some patients (Grupp et al., 2013; Maude et al., 2014; Sotillo et al., 2015; Gardner et al., 2016; Jacoby et al., 2016), outgrowth of CD19-negative tumors was detected in relapsing tumors, but interestingly, the emergence of antigen-loss variants occurred in the bone marrow, but not in lymph nodes, where tumor cells remained CD19-positive (Fig. 5, D and E). Distinct levels of immunological pressure may therefore exist in distinct organs, as we have also previously observed in a model of the graft-versus-leukemia effect (Michonneau et al., 2016). To test this idea, we compared the ability of CAR T cells to mediate the killing of transferred $CD19^+$ splenocytes in the lymph nodes and the bone marrow (Fig. 5 F). As shown in Fig. 5 G, $CD19^+$ cells

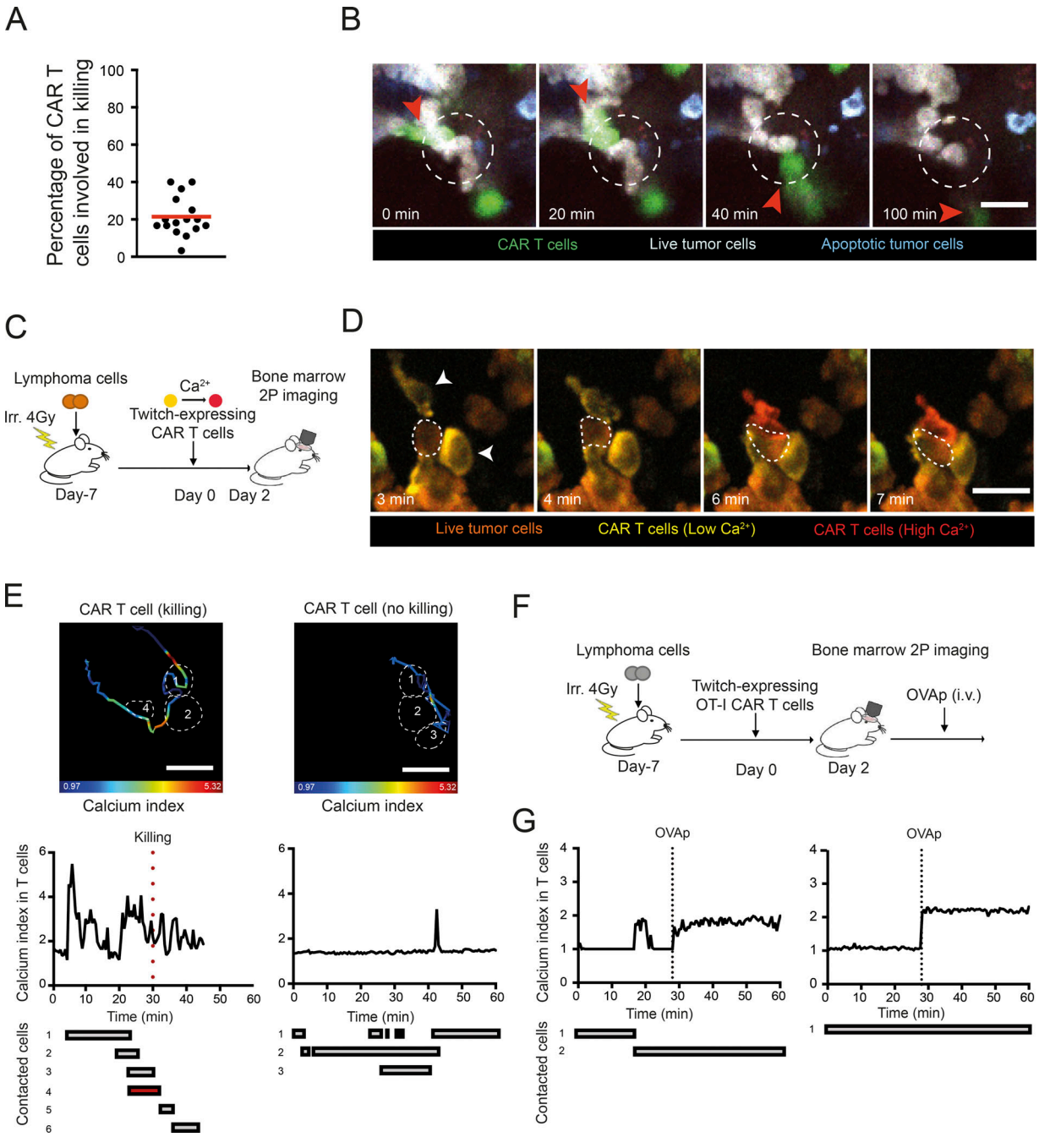

Figure 3. **Functional heterogeneity in CAR T cell–tumor interactions in the bone marrow. (A and B)** B cell lymphomas were established by i.v. injection of 0.5 × 10^6 Eμ-myc-DEVD cells in C57BL/6 mice after sublethal irradiation (4 Gy). 7 d later, mice were injected i.v. with 20 × 10^6 purified CAR T cells. Bone marrow intravital imaging was performed 40 h after T cell transfer. **(A)** The graph shows the percentage of CAR T cells involved in a direct killing event during the imaging period. Each dot represents the value calculated in one movie. Data are compiled from three independent experiments. **(B)** Representative time-lapse images illustrating that CAR T cell–tumor interactions do not necessarily lead to tumor killing. Scale bar represents 20 µm. Representative of 17 movies from three independent experiments. **(C)** Experimental setup. CAR T cell therapy was performed using CAR T cells expressing the Twitch2B genetically encoded calcium indicator. **(D and E)** Only a fraction of CAR T cell–tumor interactions trigger calcium signals in the CAR T cell. **(D)** Representative time-lapse images showing two CAR T cells (arrowheads) interacting with the same tumor cell (dotted circle) but exhibiting a different calcium response. Calcium elevation is reflected by an increase of Twitch2B FRET signal. Low and high calcium concentrations are shown in yellow and red, respectively. Tumor cells are shown in brown. Scale bar represents 20 µm. **(E)** The tracks and the color-coded calcium response of the two highlighted CAR T cells are shown (upper images). Some of the contacted tumor cells are highlighted in dotted lines. The bottom graphs show the calcium signals over time during the various contacts with tumor cells. Tumor killing is highlighted by the red dotted line. Results are representative of three independent experiments **(F and G)** CAR T cells do not exhibit a general block in calcium mobilization. Twitch2B-expressing CAR T cells were prepared from $CD8^+$ T cells bearing the OT-I transgenic TCR. During intravital imaging, $OVA^{257–264}$ peptide (OVAp) was injected i.v. The calcium responses for two representative CAR T cells are depicted, showing that CAR T cells that displayed low/no calcium signals during tumor cell contacts exhibited strong calcium responses when stimulated in vivo through their TCR. Representative of two independent experiments.

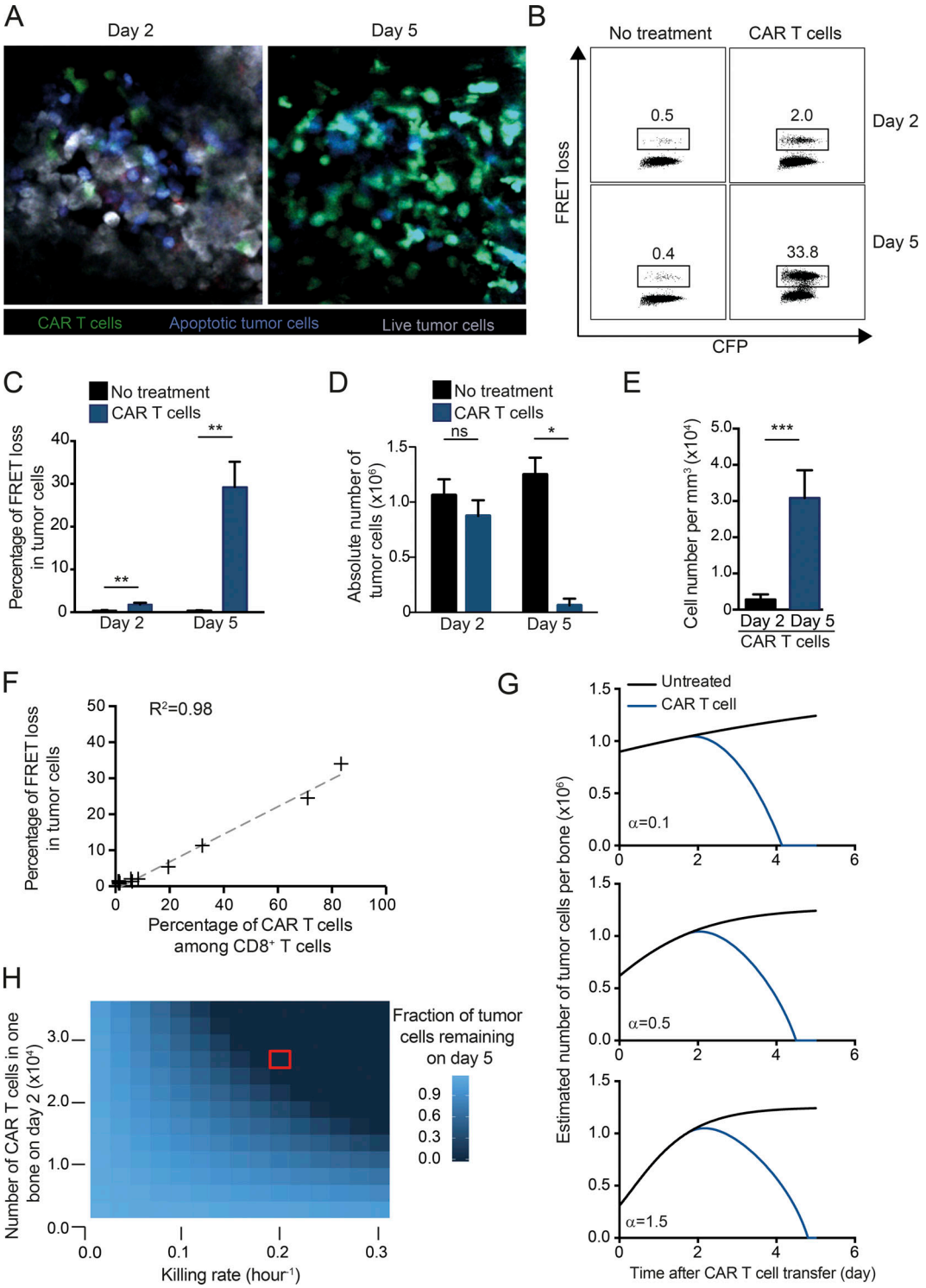

Figure 4. **CAR T cells eradicate established B cell lymphoma from the bone marrow within 5 d. (A–F)** Tumor regression during CAR T cell therapy. B cell lymphomas were established by i.v. injection of 0.5 × 10^6 Eμ-myc-DEVD cells in C57BL/6 mice after sublethal irradiation (4 Gy). 7 d later, mice were injected i.v. with 10–20 × 10^6 CAR T cells or left untreated. **(A)** Representative two-photon images of the bone marrow at days 2 and 5 after CAR T cell transfer showing the near-complete eradication of the tumor. Live cells appear in gray, apoptotic cells in blue, and CAR T cells in green. Representative of 12 images from two independent experiments. **(B–D)** Ex vivo quantification of tumor apoptosis in the bone marrow. Flow cytometry analysis was performed at days 2 and 5 after CAR T cell therapy or in the absence of treatment Representative FACS plots (B) and summary graph (C) showing the percentage of FRET loss in tumor cells. **, $P < 0.01$. **(D)** Absolute numbers of tumors cells recovered from the bone marrow of one tibia at the indicated time points. Means ± SEM are shown. *, $P < 0.05$; ns, not significant. **(E)** Bar charts showing CAR T cell density in the bone marrow quantified by two-photon imaging on days 2 and 5 after CAR T cell transfer. ***, $P < 0.001$. All data shown in B–E are representative of two independent experiments (n = 3 mice per group). **(F)** The graph shows the correlation between the percentage of FRET loss in tumor cells and the percentage of CAR T cells among total $CD8^+$ T cells. Data are compiled from several time points from two

independent experiments. Spearman's correlation coefficient is shown (R^2 = 0.98). **(G)** The tumor evolution in one bone (tibia) was modeled in the presence or absence of CAR T cells. Simulations were performed considering only the direct CAR T cell cytotoxicity and using different initial tumor growth rates (α = 0.1; α = 0.5; α = 1.5) corresponding to initial tumor doubling time of 168, 16.8, and 11.2 h respectively (see Materials and methods for details). The graphs suggest that direct killing events by CAR T cells primarily account for the rapid tumor clearance observed experimentally. **(H)** Heat map showing the tumor fate at day 5 when considering a range of killing rates and levels of CAR T cell infiltration in the bone marrow (modeled for one tibia using α = 0.5). The red square indicates the values measured experimentally.

were efficiently depleted from the bone marrow, but not from lymph nodes, despite CAR T cells being present at a higher density in lymph nodes (Fig. 5 H). Since we have previously observed in the context of allogeneic hematopoietic stem cell transplantation that differential expression of PD-1 ligands could silence CTL responses in lymph nodes, we assessed PD-L1 expression in bone marrow and lymph nodes. Consistently, we found that myeloid cells expressed high levels of PD-L1 in lymph nodes but not in the bone marrow (Fig. 5 I), suggesting that differences in tissue microenvironment may contribute to anatomical differences in CAR T cell activity. Our results suggest that CAR T cell disappearance, emergence of antigen loss variants and tumor escape in immune-privileged niches may contribute to tumor relapse after an initial near-complete elimination phase.

Concluding remarks

By imaging CAR T cell activity at the single-cell level in vivo, we have established here that the dynamics and outcomes of CAR T cell interactions are highly diverse and regulated at the functional and anatomical levels.

Cellular encounters between CAR T cells and circulating targets resulted in the rapid formation and trapping of CAR T cell clusters in the lung microcirculation. These results extend and provide a mechanistic basis for the previously described accumulation of CAR T cells in the lung in the presence of endogenous B cells (James et al., 2009). Like B cells, we found that circulating tumor cells strongly prevented CAR T cell trafficking to the bone marrow, hence representing a substantial hurdle for CAR T cell engraftment and persistence. These data provide a likely mechanism for the inverse correlation between CAR T cell persistence and circulating tumor burden observed in patients with B cell leukemias (Brentjens et al., 2011). Purging both circulating tumor and normal B cells before CAR T cell transfer using B cell–targeting treatments (antibodies or chemotherapy) may offer a clinical benefit by improving CAR T cell engraftment and persistence.

Our results strongly suggest that the fast killing dynamics of CAR T cells in vivo contribute to their therapeutic efficacy. Most killing events occurred after a single CAR T cell contact. Killing by T cell swarms and multiple contacts, which has been described previously in a viral model (Halle et al., 2016), was not preeminent in the context of CAR T cells. In addition, the rapid CAR T cell detachment seen after killing contrasts with our previous observations that conventional $CD8^+$ T cells were sequestrated by their targets long after killing in a solid tumor model (Breart et al., 2008). This feature may originate from the rapid decrease in CAR-mediated signaling associated with the formation of nonclassical immune synapses observed in a recent in vitro study (Davenport et al., 2018). Rapid detachment after target lysis could favor serial tumor cell killing. Although not preeminent, this mode of killing, which has also been observed in vitro (Davenport et al., 2015; Liadi et al., 2015), contributed to the efficacy of CAR T cells in vivo. Notably, not all CAR T cells were engaged in cytotoxic activity during the imaging periods. This heterogeneity was reflected at the level of signaling, with some CAR T cells failing to trigger a sustained calcium mobilization upon tumor cell interactions. CAR down-regulation, downstream signaling defects, or expression of inhibitory receptors may possibly contribute to this heterogeneity. Despite the diversity in the outcome of CAR T cell contacts, we provide experimental and mathematical evidence for a near-complete tumor elimination within 5 d mediated by direct killing events. The rapid killing dynamics of at least a fraction of CAR T cells, together with the progressive accumulation of CAR T cells in the bone marrow, were key features that accounted for tumor clearance. While our study primarily focused on $CD8^+$ CAR T cells, it will be interesting to investigate whether $CD4^+$ CAR T cells exhibit similar killing activity and dynamics.

We show that tumor immunoediting can be site specific, highlighting the importance of understanding how antitumor responses are regulated at the organ level. In particular, our data suggest anatomical differences in the levels of CAR T cell–mediated immunological pressure. In particular, CAR T cell activity is limited in lymph nodes and is associated with a more suppressive microenvironment. These findings, together with our previous observations in a model of the graft-versus-leukemia effect (Michonneau et al., 2016), suggest that the lymph nodes may represent a niche for B cell lymphoma to escape immune surveillance. It is tempting to speculate that such anatomical differences in CAR T cell activity may account for the reduced response rates and delayed efficacy seen in patients with B cell lymphoma as compared with acute leukemia (Neelapu et al., 2017; Schuster et al., 2017; Maude et al., 2018; Park et al., 2018).

In sum, our results establish the large diversity in CAR T cell contact outcomes in distinct anatomical sites impacting engraftment, antitumor activity, and tumor immunoediting. As illustrated here, defining the relevant immune cell interactions at the anatomical and microanatomical levels represents an essential step toward a mechanistic understanding of tumor immunotherapies and identifying strategies for treatment optimization.

Materials and methods

Mice and cell lines

6–8-wk-old C57BL/6J mice were purchased from Charles River. OT-I TCR, Ubi-GFP, Ubi-GFP $RAG1^{-/-}$ OT-I TCR, $CD19^{cre}$xRosa26-RFP, Eμ-myc, and $RAG2^{-/-}$ mice were bred in our animal facility

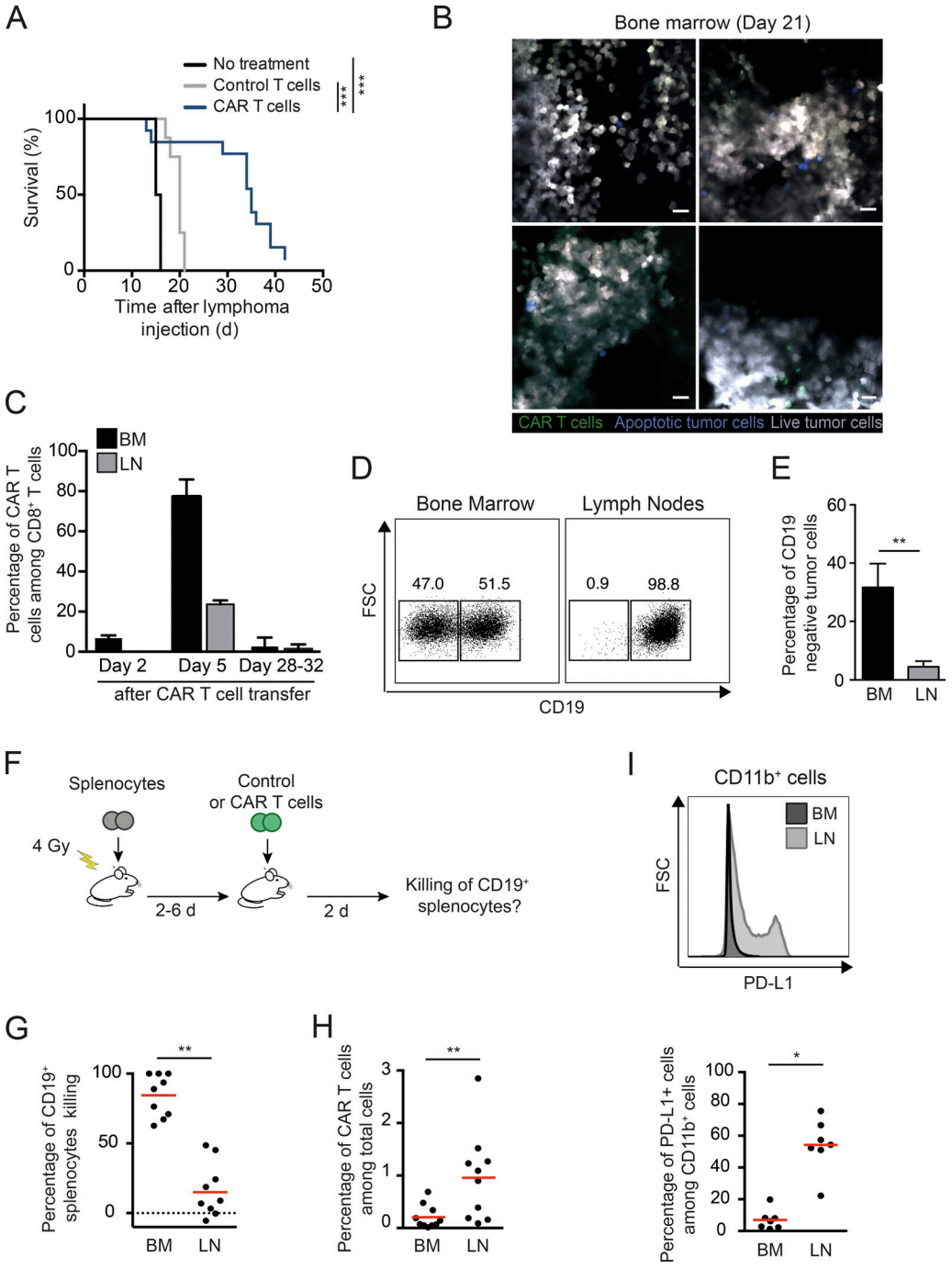

Figure 5. **Site-specific tumor immunoediting following CAR T cell therapy. (A–E)** B cell lymphomas were established by i.v. injection of 0.5 × 10^6 Eμ-myc-DEVD cells in C57BL/6 mice after sublethal irradiation (4 Gy). 7 d later, mice were injected i.v. with CAR T cells or control activated T cells (untransduced) or left untreated. **(A)** CAR T cell therapy prolongs mice survival. Log-rank test was used for statistical analysis. ***, P < 0.001. Data are compiled from three independent experiments (*n* = 8 mice in the control group and *n* = 13 mice in the CAR T cell group). **(B)** Representative images of the bone marrow on day 21 after CAR T cell therapy. Images show massive tumor infiltration (live tumor cells in gray), a few occasional CAR T cells (green), and rare apoptotic tumors (blue). Representative of 16 images from two independent experiments. Scale bars represent 20 μm. **(C)** Disappearance of CAR T cells at late time points. Bar charts showing the percentage of CAR T cells among $CD8^+$ T cells at the indicated time points in the bone marrow (BM) and in lymph nodes (LN). Data are compiled from several time points from three independent experiments (*n* = 3 mice per group). **(D and E)** Emergence of CD19-negative tumor cells is detected in the bone marrow but not in lymph nodes. Representative FACS plots (D) and bar charts (E) showing CD19 expression in tumors cells (identified based on their fluorescence) in the bone marrow and lymph nodes. Analyses were performed between days 28 and 32. Data are compiled from three independent experiments. FSC, forward scatter. Mann–Whitney test was for statistical analysis. **, P < 0.01. **(F–H)** CAR T cell exhibit a reduced cytotoxic activity in lymph nodes. **(F)** Experimental setup. **(G)** The in vivo killing of transferred $CD19^+$ splenocytes was compared in the bone marrow and lymph nodes. **(H)** Frequency of CAR T cells among total cells as analyzed by flow cytometry. **(I)** Strong PD-L1 expression in myeloid cells is detected in the lymph nodes, but not the bone marrow, following CAR T cell therapy. Representative histograms (upper panel) and compiled quantification (lower graph). Each dot represents one mouse. Data are compiled from three independent experiments. Wilcoxon matched-pairs signed rank test was used for statistical analysis. **, P < 0.01; *, P < 0.05.

under specific pathogen–free conditions. All animal studies were approved by the Institut Pasteur Safety Committee in accordance with French and European guidelines (CETEA 2013–0077). A Burkitt-like lymphoma B cell line was isolated from male Eμ-myc mice and transduced to express a FRET-based reporter for caspase-3 activity (Eμ-myc-DEVD line; Michonneau et al., 2016). Mice were examined every day and sacrificed in case of prostration, tousled hair, weakness, ectopic, or nodal tumor mass >1 cm.

CAR T cell generation, adoptive transfer, and combined in vivo anti-CD20 therapy

The tCD34.2A.amCD19.CD28IEVζ retroviral vector encoding anti-CD19 CAR has been described previously (Cheadle et al., 2014). Briefly, the CAR construct is composed of the anti-murine CD19 single-chain fragment variable domain derived from the 1D3 rat hybridoma, the transmembrane and intracellular domains of CD28, and the CD3ζ intracellular domain. The retroviral vector also encodes the human CD34 molecule used for identification and purification of CAR T cells. $CD8^+$ T cells were isolated from lymph nodes of Ubi-GFP OT-I TCR $RAG1^{-/-}$ or Ubi-GFP mice using a CD8-negative selection kit (Miltenyi). T cells were activated in plates coated with 2.5 μg anti-CD3 mAb (clone 17.A2; BioLegend) in the presence of 2.5 μg/ml soluble anti-CD28 mAb (clone 37.51; BioLegend) and 10 ng/ml murine IL-12 (Andrijauskaite et al., 2015; SRP3204; Sigma-Aldrich). Two rounds of spin-infection were performed at 24 and 48 h after T cell activation using retroviral particles supplemented with 8 μg/ml polybrene (Merck). T cells were cultured for 4 additional days in the presence of 25 IU/ml hIL-2 (11147528001; Roche). When indicated, T cells were also transduced to express the Twitch2B genetically encoded calcium reporter (Thestrup et al., 2014). Untransduced control T cells were activated and cultured in the same conditions. Purification of transduced cells was performed using hCD34 positive selection kit (Miltenyi). Burkitt-like B cell lymphoma was established in the bone marrow and lymph nodes by i.v. injection of 0.5×10^6 Eμ-myc cells in C57BL/6 mice after sublethal irradiation (4 Gy), used as a conditioning regimen for CAR T cell engraftment (Kochenderfer et al., 2010). After 7–11 d (when lymphoma cells were detected in the blood), mice were injected with $10–20 \times 10^6$ CAR T cells or control T cells. In combination therapy experiments, mice received 50 μg anti-CD20 monoclonal antibody (5D2, mIgG2a; Genentech) once a week, starting 3 d before CAR T cell transfer.

Flow cytometry

Cell suspensions were Fc blocked using anti-CD16/32 mAbs (clone 93; BioLegend) and normal murine serum 1%. Stainings were performed with the following mAbs: hCD34-BV421 or Alexa Fluor 647 (561; BioLegend), CD3e-BUV395 (145-2C11; BioLegend) or CD8-BUV395 (53–6.7; BioLegend), PD-1 Pe/Cy7 (J43; BioLegend), CD19-APC-fire750 (6D5; BioLegend), or PD-L1-PE (10F.9G2; BioLegend). Intracellular stainings were performed on CAR or control T cells cultured in the presence or absence of target cells for 20 h using the Cytofix/Cytoperm kit (BD Biosciences), Allophycocyanin-conjugated anti-Granzyme B mAb (GB11; BioLegend) or Alexa Fluor 647–conjugated anti-IFN-γ mAb (clone XMG1.2; eBioscience). IFN-γ expression was assayed in the presence of 1 μg/ml Brefeldin A (BD Biosciences). Analyses were performed with a FACSCanto II cytometer (BD Biosciences) or an LSR/Fortessa (BD Biosciences) and analyzed with FlowJo software version 10.1 (Tree Star). FRET loss was defined as a derived parameter using the ratio of CFP to FRET fluorescence. FRET loss was measured on cells fixed with 2% paraformaldehyde solution (Sigma) immediately after isolation.

Two-photon imaging

Bone marrow intravital imaging was performed 40 h after T cell transfer by adapting a previously described protocol (Mazo et al., 1998). Briefly, mice were anesthetized with a mixture of xylazine (Rompun, 10 mg/kg) and ketamine (Imalgene, 100 mg/kg). The scalp hair was removed, and the scalp was incised at the midline and then exposed. The jaw was fixed on the surface of a steel plate to maintain the superior part of the skull horizontally, and a round 20-mm coverslip was centered and fixed above the frontoparietal suture after PBS deposition using a cyanoacrylate-based glue. During imaging, mice were supplied with oxygen, and their temperature was maintained at 37°C with a heating pad. Two-photon imaging was performed with an upright microscope FVMPE-RS (OLYMPUS) and a 25×/1.05 NA water-dipping objective (OLYMPUS). Excitation was provided by an Insight deep see dual laser (Spectra Physics) tuned at 880 nm. CFP and FRET were detected using 483/32 and 542/27 filters, respectively. To create time-lapse sequences, we typically scanned a 30-μm-thick volume of tissue at 5-μm Z-steps and 60-s intervals. Videos were processed and analyzed with Imaris software (Bitplane) or Fiji software (1.49 m; ImageJ). Videos and figures based on two-photon microscopy are shown as two-dimensional maximum intensity projections of three-dimensional data. Analysis of contact duration during killing was restricted to events in which initial encounter could be imaged. Pulmonary lobes were imaged ex vivo on a Petri dish topped by a round 20-mm coverslip.

Mathematical modeling of tumor dynamics during CAR T cell therapy

We modeled the growth of tumors and their destruction by CAR T cells by considering cells and their interactions within the bone marrow compartment of a single bone (based on a combination of imaging and flow cytometry measurements made on tibias).

Tumor growth was described with the Gompertz model, which is a classical ordinary differential equation model in which the tumor growth rate slows down exponentially over time. This implies that the tumor growth rate is higher for small tumors than for large tumors, thus also taking into account a potential increase of tumor proliferation during CAR T cell therapy due to cleared bone marrow niches. Similar to Murphy et al. (2016), we reparameterized the Gompertz model in terms of initial cell numbers and included a term to describe killing by CAR T cells:

$$\frac{dB}{dt} = B\left[\alpha - \beta \ln\left(\frac{B}{B_0}\right)\right] - kC,$$

where B represents the number of tumor B cells, B_0 is the number of tumor cells at day 0 (time of CAR T cell transfer), α represents the initial growth rate of the tumor, β describes the rate at which tumor growth slows, C represents the number of CAR T cells, and k represents the killing rate per CAR T cell.

In the absence of CAR T cells, no killing occurs and an analytical solution to this model (Benzekry et al., 2014) is

$$B(t) = B_0 e^{\frac{\alpha}{\beta}\left(1-e^{-\beta t}\right)}.$$

Based on measurements of absolute tumor cell numbers on days 2 and 5 (Fig. 4 D; the latter exhibiting a 17% increase in tumor size compared with the former, corresponding to a growth rate of 0.054 d^{-1}) in the absence of CAR T cell treatment, we set boundary conditions for B_2 and for $\frac{B_5}{B_2}$. For each initial growth rate α, the analytical solution can be solved simultaneously with these boundary conditions to determine unique values for B_0 and β.

To determine the killing rate around day 2 based on our in-vivo imaging data, we divided the observed number of apoptotic events due to direct killing by the number of CAR T cells observed in the movie (13 movies were analyzed). The average of these killing rates per video was equal to 0.2 kills CAR^{-1} h^{-1}, which we used as a default value for k. Killing of targets by T cells is expected to saturate with increasing cell densities, which can be described with a general saturation function (Gadhamsetty et al., 2014). However, early after CAR infusion, individual T cells encounter a surplus of tumor cells and are therefore expected to kill at their maximum rate. The general saturation function in that case reduces to the killing term we applied here (Gadhamsetty et al., 2014; i.e., −kC). At later stages the killing rate per CAR T cell may decrease, but this would occur only at a stage where the tumor is already controlled by CAR T cells and does not affect the overall conclusions with respect to tumor control.

We included the increase in CAR T cell numbers into the simulations with the ordinary differential equation model, which was based on the data shown in Fig. 4 E. Specifically, the increase in average number of intratumoral CAR T cells over time was considered to be linear according to the following relation:

$$C(t) = max\left(\frac{C_5 - C_2}{3}t + C_2 - \frac{2(C_5 - C_2)}{3}, 0\right),$$

where C_2 and C_5 are the average observed numbers of CAR T cells at day 2 (40 h) and day 5 (112 h), respectively. The term $\frac{C_5-C_2}{3}$ corresponds to the daily increase in CAR T cells (assumed to be linear).

Simulations were run for different initial tumor growth rates in order to investigate the sensitivity of the results to that unknown parameter. Moreover, the killing rate and the infiltration rate of CAR T cells were varied in order to investigate the importance of these parameters in regression of the tumor. The model parameters inferred from the three tested initial growth rates (see Fig. 4 G) were: [α = 0.1, β = 0.19, B_0 = 898000]; [α =0.5, β = 0.695, B_0 = 618000]; [α =1.5, β = 1.07, B_0 = 309000]. All simulations were run in R (version 3.3.2) using the package deSolve (version 1.14).

Statistical analysis

All statistical tests were performed with Prism v.6.0b (GraphPad). *t*, Mann–Whitney, or Kruskal–Wallis tests were used as indicated, and Dunn's test was used for multiple comparisons correction. Data are expressed as mean ± SEM.

Online supplemental material

Fig. S1 shows the detection of CAR T cells mediated tumor killing in vitro using a genetically encoded apoptosis reporter. Fig. S2 shows that removal of circulating B cells increases CAR T cell activity. Fig. S3 compares CAR T cell and OT-I T cell killing in vitro and in vivo. Video 1 shows intravital bone marrow imaging of lymphoma-bearing mice treated with control T cells. Videos 2 and 3 illustrate efficient and rapid killing of B cell tumors by CAR T cells in the bone marrow. Video 4 highlights an example of a B cell tumor undergoing apoptosis without apparent CAR T cell contacts. Video 5 shows CAR T cell serial killing of adjacent tumor cells in the bone marrow. Video 6 shows an example of a CAR T cell forming prolonged interactions with tumor cells without inducing their apoptosis. Video 7 highlights a CAR T cell with high calcium responses upon interactions with tumor cells. Video 8 shows an example of CAR T cell with weak calcium responses upon interactions with tumor cells.

Acknowledgments

We thank members of the Bousso laboratory for critical review of the manuscript. We acknowledge the mouse facility and Technology Core of the Center for Translational Science at Institut Pasteur for support in conducting this study.

This work was supported by Institut Pasteur, INSERM, the European Research Council (starting [Lymphocytecontact] and advanced grants [ENLIGHTEN] to P. Bousso), and the NWO (Vidi grant 864.12.013 to J.B. Beltman). M. Cazaux received financial support from ITMO Cancer Alliance Nationale pour les Sciences de la Vie et de la Santé within the framework of the Cancer Plan.

The authors declare no competing financial interests.

Author contributions: M. Cazaux, C.L. Grandjean, F. Lemaître, and J. Postat conducted the experiments. Z. Garcia and I. Milo contributed to intravital imaging experiments. E.J. Cheadle, provided critical reagents. R.J. Beck and J.B. Beltman designed mathematical modeling, and R.J. Beck performed mathematical modeling. M. Cazaux, C.L. Grandjean, and P. Bousso designed the experiments. M. Cazaux, C.L. Grandjean, R.J. Beck, J.B. Beltman, and P. Bousso analyzed the data and wrote the manuscript.

Submitted: 21 December 2018
Revised: 7 February 2019
Accepted: 4 March 2019

References

Adams, J.M., A.W. Harris, C.A. Pinkert, L.M. Corcoran, W.S. Alexander, S. Cory, R.D. Palmiter, and R.L. Brinster. 1985. The c-myc oncogene driven by immunoglobulin enhancers induces lymphoid malignancy in transgenic mice. *Nature.* 318:533–538. https://doi.org/10.1038/318533a0

Andrijauskaite, K., S. Suriano, C.A. Cloud, M. Li, P. Kesarwani, L.S. Stefanik, K.M. Moxley, M.L. Salem, E. Garrett-Mayer, C.M. Paulos, et al. 2015. IL-12 conditioning improves retrovirally mediated transduction efficiency of CD8+ T cells. *Cancer Gene Ther.* 22:360–367. https://doi.org/10.1038/cgt.2015.28

Barber, A., A. Rynda, and C.L. Sentman. 2009. Chimeric NKG2D expressing T cells eliminate immunosuppression and activate immunity within the ovarian tumor microenvironment. *J. Immunol.* 183:6939–6947. https://doi.org/10.4049/jimmunol.0902000

Benzekry, S., C. Lamont, A. Beheshti, A. Tracz, J.M. Ebos, L. Hlatky, and P. Hahnfeldt. 2014. Classical mathematical models for description and prediction of experimental tumor growth. *PLOS Comput. Biol.* 10: e1003800. https://doi.org/10.1371/journal.pcbi.1003800

Breart, B., F. Lemaître, S. Celli, and P. Bousso. 2008. Two-photon imaging of intratumoral CD8+ T cell cytotoxic activity during adoptive T cell therapy in mice. *J. Clin. Invest.* 118:1390–1397. https://doi.org/10.1172/JCI34388

Brentjens, R.J., I. Rivière, J.H. Park, M.L. Davila, X. Wang, J. Stefanski, C. Taylor, R. Yeh, S. Bartido, O. Borquez-Ojeda, et al. 2011. Safety and persistence of adoptively transferred autologous CD19-targeted T cells in patients with relapsed or chemotherapy refractory B-cell leukemias. *Blood.* 118:4817–4828. https://doi.org/10.1182/blood-2011-04-348540

Cheadle, E.J., R.E. Hawkins, H. Batha, A.L. O'Neill, S.J. Dovedi, and D.E. Gilham. 2010. Natural expression of the CD19 antigen impacts the long-term engraftment but not antitumor activity of CD19-specific engineered T cells. *J. Immunol.* 184:1885–1896. https://doi.org/10.4049/jimmunol.0901440

Cheadle, E.J., V. Sheard, D.G. Rothwell, J.S. Bridgeman, G. Ashton, V. Hanson, A.W. Mansoor, R.E. Hawkins, and D.E. Gilham. 2014. Differential role of Th1 and Th2 cytokines in autotoxicity driven by CD19-specific second-generation chimeric antigen receptor T cells in a mouse model. *J. Immunol.* 192:3654–3665. https://doi.org/10.4049/jimmunol.1302148

Chmielewski, M., C. Kopecky, A.A. Hombach, and H. Abken. 2011. IL-12 release by engineered T cells expressing chimeric antigen receptors can effectively Muster an antigen-independent macrophage response on tumor cells that have shut down tumor antigen expression. *Cancer Res.* 71:5697–5706. https://doi.org/10.1158/0008-5472.CAN-11-0103

Davenport, A.J., M.R. Jenkins, R.S. Cross, C.S. Yong, H.M. Prince, D.S. Ritchie, J.A. Trapani, M.H. Kershaw, P.K. Darcy, and P.J. Neeson. 2015. CAR-T Cells Inflict Sequential Killing of Multiple Tumor Target Cells. *Cancer Immunol. Res.* 3:483–494. https://doi.org/10.1158/2326-6066.CIR-15-0048

Davenport, A.J., R.S. Cross, K.A. Watson, Y. Liao, W. Shi, H.M. Prince, P.A. Beavis, J.A. Trapani, M.H. Kershaw, D.S. Ritchie, et al. 2018. Chimeric antigen receptor T cells form nonclassical and potent immune synapses driving rapid cytotoxicity. *Proc. Natl. Acad. Sci. USA.* 115:E2068–E2076. https://doi.org/10.1073/pnas.1716266115

Gadhamsetty, S., A.F. Marée, J.B. Beltman, and R.J. de Boer. 2014. A general functional response of cytotoxic T lymphocyte-mediated killing of target cells. *Biophys. J.* 106:1780–1791. https://doi.org/10.1016/j.bpj.2014.01.048

Gardner, R., D. Wu, S. Cherian, M. Fang, L.A. Hanafi, O. Finney, H. Smithers, M.C. Jensen, S.R. Riddell, D.G. Maloney, and C.J. Turtle. 2016. Acquisition of a CD19-negative myeloid phenotype allows immune escape of MLL-rearranged B-ALL from CD19 CAR-T-cell therapy. *Blood.* 127: 2406–2410. https://doi.org/10.1182/blood-2015-08-665547

Garrod, K.R., H.D. Moreau, Z. Garcia, F. Lemaître, I. Bouvier, M.L. Albert, and P. Bousso. 2012. Dissecting T cell contraction in vivo using a genetically encoded reporter of apoptosis. *Cell Reports.* 2:1438–1447. https://doi.org/10.1016/j.celrep.2012.10.015

Grupp, S.A., M. Kalos, D. Barrett, R. Aplenc, D.L. Porter, S.R. Rheingold, D.T. Teachey, A. Chew, B. Hauck, J.F. Wright, et al. 2013. Chimeric antigen receptor-modified T cells for acute lymphoid leukemia. *N. Engl. J. Med.* 368:1509–1518. https://doi.org/10.1056/NEJMoa1215134

Halle, S., K.A. Keyser, F.R. Stahl, A. Busche, A. Marquardt, X. Zheng, M. Galla, V. Heissmeyer, K. Heller, J. Boelter, et al. 2016. In Vivo Killing Capacity of Cytotoxic T Cells Is Limited and Involves Dynamic Interactions and T Cell Cooperativity. *Immunity.* 44:233–245. https://doi.org/10.1016/j.immuni.2016.01.010

Harris, A.W., C.A. Pinkert, M. Crawford, W.Y. Langdon, R.L. Brinster, and J.M. Adams. 1988. The E mu-myc transgenic mouse. A model for high-incidence spontaneous lymphoma and leukemia of early B cells. *J. Exp. Med.* 167:353–371. https://doi.org/10.1084/jem.167.2.353

Jacoby, E., S.M. Nguyen, T.J. Fountaine, K. Welp, B. Gryder, H. Qin, Y. Yang, C.D. Chien, A.E. Seif, H. Lei, et al. 2016. CD19 CAR immune pressure induces B-precursor acute lymphoblastic leukaemia lineage switch exposing inherent leukaemic plasticity. *Nat. Commun.* 7:12320. https://doi.org/10.1038/ncomms12320

James, S.E., N.N. Orgun, T.F. Tedder, M.J. Shlomchik, M.C. Jensen, Y. Lin, P.D. Greenberg, and O.W. Press. 2009. Antibody-mediated B-cell depletion before adoptive immunotherapy with T cells expressing CD20-specific chimeric T-cell receptors facilitates eradication of leukemia in immunocompetent mice. *Blood.* 114:5454–5463. https://doi.org/10.1182/blood-2009-08-232967

Kochenderfer, J.N., Z. Yu, D. Frasheri, N.P. Restifo, and S.A. Rosenberg. 2010. Adoptive transfer of syngeneic T cells transduced with a chimeric antigen receptor that recognizes murine CD19 can eradicate lymphoma and normal B cells. *Blood.* 116:3875–3886. https://doi.org/10.1182/blood-2010-01-265041

Liadi, I., H. Singh, G. Romain, N. Rey-Villamizar, A. Merouane, J.R. Adolacion, P. Kebriaei, H. Huls, P. Qiu, B. Roysam, et al. 2015. Individual Motile CD4(+) T Cells Can Participate in Efficient Multikilling through Conjugation to Multiple Tumor Cells. *Cancer Immunol. Res.* 3:473–482. https://doi.org/10.1158/2326-6066.CIR-14-0195

Maude, S.L., N. Frey, P.A. Shaw, R. Aplenc, D.M. Barrett, N.J. Bunin, A. Chew, V.E. Gonzalez, Z. Zheng, S.F. Lacey, et al. 2014. Chimeric antigen receptor T cells for sustained remissions in leukemia. *N. Engl. J. Med.* 371: 1507–1517. https://doi.org/10.1056/NEJMoa1407222

Maude, S.L., T.W. Laetsch, J. Buechner, S. Rives, M. Boyer, H. Bittencourt, P. Bader, M.R. Verneris, H.E. Stefanski, G.D. Myers, et al. 2018. Tisagenlecleucel in Children and Young Adults with B-Cell Lymphoblastic Leukemia. *N. Engl. J. Med.* 378:439–448. https://doi.org/10.1056/NEJMoa1709866

Mazo, I.B., J.C. Gutierrez-Ramos, P.S. Frenette, R.O. Hynes, D.D. Wagner, and U.H. von Andrian. 1998. Hematopoietic progenitor cell rolling in bone marrow microvessels: parallel contributions by endothelial selectins and vascular cell adhesion molecule 1. *J. Exp. Med.* 188:465–474. https://doi.org/10.1084/jem.188.3.465

Michonneau, D., P. Sagoo, B. Breart, Z. Garcia, S. Celli, and P. Bousso. 2016. The PD-1 Axis Enforces an Anatomical Segregation of CTL Activity that Creates Tumor Niches after Allogeneic Hematopoietic Stem Cell Transplantation. *Immunity.* 44:143–154. https://doi.org/10.1016/j.immuni.2015.12.008

Murphy, H., H. Jaafari, and H.M. Dobrovolny. 2016. Differences in predictions of ODE models of tumor growth: a cautionary example. *BMC Cancer.* 16:163. https://doi.org/10.1186/s12885-016-2164-x

Neelapu, S.S., F.L. Locke, N.L. Bartlett, L.J. Lekakis, D.B. Miklos, C.A. Jacobson, I. Braunschweig, O.O. Oluwole, T. Siddiqi, Y. Lin, et al. 2017. Axicabtagene Ciloleucel CAR T-Cell Therapy in Refractory Large B-Cell Lymphoma. *N. Engl. J. Med.* 377:2531–2544. https://doi.org/10.1056/NEJMoa1707447

Park, J.H., I. Rivière, M. Gonen, X. Wang, B. Sénéchal, K.J. Curran, C. Sauter, Y. Wang, B. Santomasso, E. Mead, et al. 2018. Long-Term Follow-up of CD19 CAR Therapy in Acute Lymphoblastic Leukemia. *N. Engl. J. Med.* 378:449–459. https://doi.org/10.1056/NEJMoa1709919

Ruella, M., and M.V. Maus. 2016. Catch me if you can: Leukemia Escape after CD19-Directed T Cell Immunotherapies. *Comput. Struct. Biotechnol. J.* 14: 357–362. https://doi.org/10.1016/j.csbj.2016.09.003

Schuster, S.J., J. Svoboda, E.A. Chong, S.D. Nasta, A.R. Mato, Ö. Anak, J.L. Brogdon, I. Pruteanu-Malinici, V. Bhoj, D. Landsburg, et al. 2017. Chimeric Antigen Receptor T Cells in Refractory B-Cell Lymphomas. *N. Engl. J. Med.* 377:2545–2554. https://doi.org/10.1056/NEJMoa1708566

Sotillo, E., D.M. Barrett, K.L. Black, A. Bagashev, D. Oldridge, G. Wu, R. Sussman, C. Lanauze, M. Ruella, M.R. Gazzara, et al. 2015. Convergence of Acquired Mutations and Alternative Splicing of CD19 Enables Resistance to CART-19 Immunotherapy. *Cancer Discov.* 5:1282–1295. https://doi.org/10.1158/2159-8290.CD-15-1020

Thestrup, T., J. Litzlbauer, I. Bartholomäus, M. Mues, L. Russo, H. Dana, Y. Kovalchuk, Y. Liang, G. Kalamakis, Y. Laukat, et al. 2014. Optimized ratiometric calcium sensors for functional in vivo imaging of neurons and T lymphocytes. *Nat. Methods.* 11:175–182. https://doi.org/10.1038/nmeth.2773

Yeku, O.O., T.J. Purdon, M. Koneru, D. Spriggs, and R.J. Brentjens. 2017. Armored CAR T cells enhance antitumor efficacy and overcome the tumor microenvironment. *Sci. Rep.* 7:10541. https://doi.org/10.1038/s41598-017-10940-8